

Electronic Supplementary Information

Porous Hierarchical Nickel Nanostructures and their Application as Magnetically Separable Catalyst

Jingfang Xiong, Hu Shen, Junxian Mao, Xingtai Qin, Pei Xiao, Xizhang Wang, Qiang Wu,* and Zheng Hu

Key Laboratory of Mesoscopic Chemistry of MOE and Jiangsu Provincial Lab for Nanotechnology, School of Chemistry and Chemical Engineering, Nanjing University, Nanjing, 210093 (China)

E-mail: wqchem@nju.edu.cn.

Index

- SI-1. FTIR spectrum of the nanostructured precursor
- SI-2. Two control experiments
- SI-3. Characterizations on the porous NiO microflowers
- SI-4. Typical SEM image of Ni-335°C sample
- SI-5. In situ DTG curves and MS spectra in calcining the precursors in Ar and air
- SI-6. Magnetic properties of the Ni nanostructures
- SI-7. Characterization on Ni-335°C catalyst after reaction

Reference

SI-1. FTIR spectrum of the nanostructured precursor

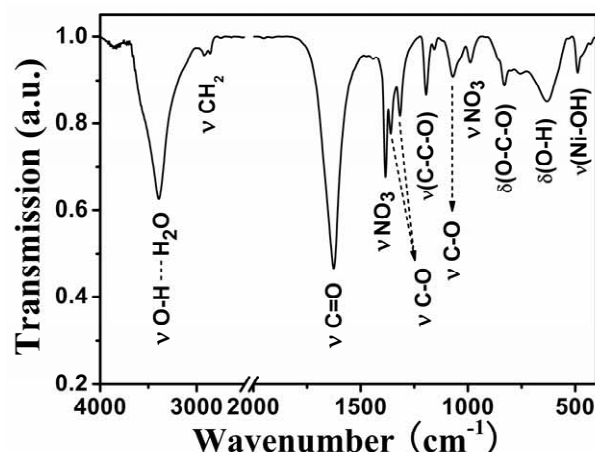


Fig. S1 FTIR spectrum of the flowerlike precursor.

α-Ni(OH)₂: The bands at ca. 3393 cm⁻¹, 633 cm⁻¹ and 488 cm⁻¹ could be assigned to the ν(O-H), δ(O-H) and ν(Ni-OH) vibrations of Ni(OH)₂, respectively.¹⁻³ No sharp peak at ca. 3600 cm⁻¹ is observed, suggesting the absence of β-Ni(OH)₂.⁴ In combination with the XRD result (Fig. 1d in the main text), it is learnt the nickel hydroxide presents as α-Ni(OH)₂.

NiC₂O₄: The bands at 1620 cm⁻¹, 829 cm⁻¹ and 1193 cm⁻¹ could be assigned to the asymmetric ν(C=O) and δ(O-C-O), and the symmetric ν(C-C-O) vibrations of NiC₂O₄, respectively. The bands at 1358 cm⁻¹ and 1315 cm⁻¹ could be ascribed to the symmetric ν(C-O) vibrations, which suggest the bridging oxalates are coordinated to nickel atoms with all four oxygen atoms.⁵

HCHO: Two peaks centered at ca. 2925 cm⁻¹ and 2850 cm⁻¹ as well as the peak at 1070 cm⁻¹ could be ascribed to the ν(CH₂) and ν(C-O) vibrations, in accordance with the standard IR spectrum of HCHO.

NO₃⁻: The sharp bands at 1385 cm⁻¹ and 989 cm⁻¹ could validate the presence of NO₃⁻.^{2,6}

SI-2. Two control experiments

To learn the formation of the nanostructured Ni-based precursor, two control experiments were carried out. Briefly, only H₂C₂O₄·2H₂O or hexamethylenetetramine (HMT) was used as the precipitator to prepare two control precursors while keeping the other preparation conditions the same as that for preparing the precursor in the main text. TEM images and XRD patterns show that the control precursor with H₂C₂O₄·2H₂O precipitator is the microsized particles of NiC₂O₄·2H₂O (Fig. S2a, c), whereas that with HMT precipitator is the flowerlike Ni(OH)₂ (both α- and β- phase) microspheres with sparse cores (Fig. S2b, d). We noted that the formation of NiC₂O₄·2H₂O started at ca. 80 °C; while that of Ni(OH)₂ was obviously more difficult, i.e., at ca. 100 °C after about 10 min reflux of the reaction solution. Thus, in comparison with the morphology and components of the precursor microflowers in Fig. 1 (see the main text), it is learnt that the precursor microflowers in Fig. 1a are made of the solid cores of NiC₂O₄·2H₂O and the petal-like shells of α-Ni(OH)₂. The formation of the precursor microflowers should like this: NiC₂O₄ particles were formed at the temperature

above 80 °C through the reaction between $\text{Ni}(\text{NO}_3)_2$ and $\text{H}_2\text{C}_2\text{O}_4 \cdot \text{H}_2\text{O}$. When the temperature was further raised to 100 °C, HMT was hydrolyzed gradually into NH_3 and HCHO , and then $\text{NH}_3 \cdot \text{H}_2\text{O}$ reacted with Ni^{2+} to produce $\alpha\text{-Ni(OH)}_2$ microflowers based on the nuclei of NiC_2O_4 particles similar to the case in the literature.³

The HCHO molecules and NO_3^- ions in the Ni-based precursor (see Fig. S1) were mainly intercalated into the $\alpha\text{-Ni(OH)}_2$ with layered structure,³ as revealed by the follow experiments. By calcining the control precursor of the flowerlike Ni(OH)_2 in Ar at 340 °C, NiO and Ni were obtained (Fig. S2e). This indicates the existence of some reducer in the control precursor; otherwise only NiO would be obtained from the decomposition of Ni(OH)_2 . According to the preparation of the control precursor, the reducer should be HCHO molecules from the hydrolysis of HMT, which is confirmed by the detected species of CO^+ (28 amu) and CO_2^+ (44 amu) during the in situ TG-DSC-MS analysis on the pyrolysis of the control precursor in Ar (inset in Fig. S2e). The NO^+ (30 amu) signal was also detected (inset in Fig. S2e), which came from the decomposition of the intercalated NO_3^- .

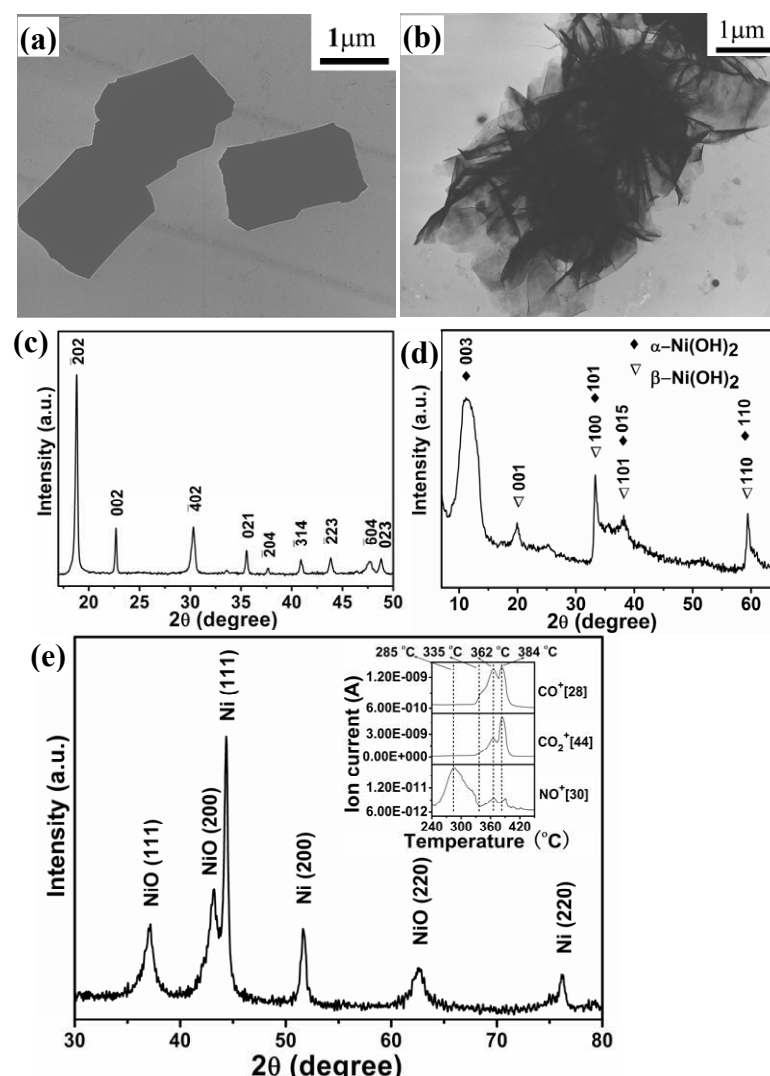


Fig. S2 TEM images and XRD patterns of the control precursors using only oxalic acid (a, c) or HMT (b, d) as the precipitator. (e) XRD pattern of the product obtained by heat-treating the control precursor in (b, d) in Ar at 340 °C. Inset is the detected CO^+ (28 amu), CO_2^+ (44 amu)

and NO^+ (30 amu) species during the in situ TG-DSC-MS analysis on the pyrolysis of this control precursor in Ar.

SI-3. Characterizations on the porous NiO microflowers

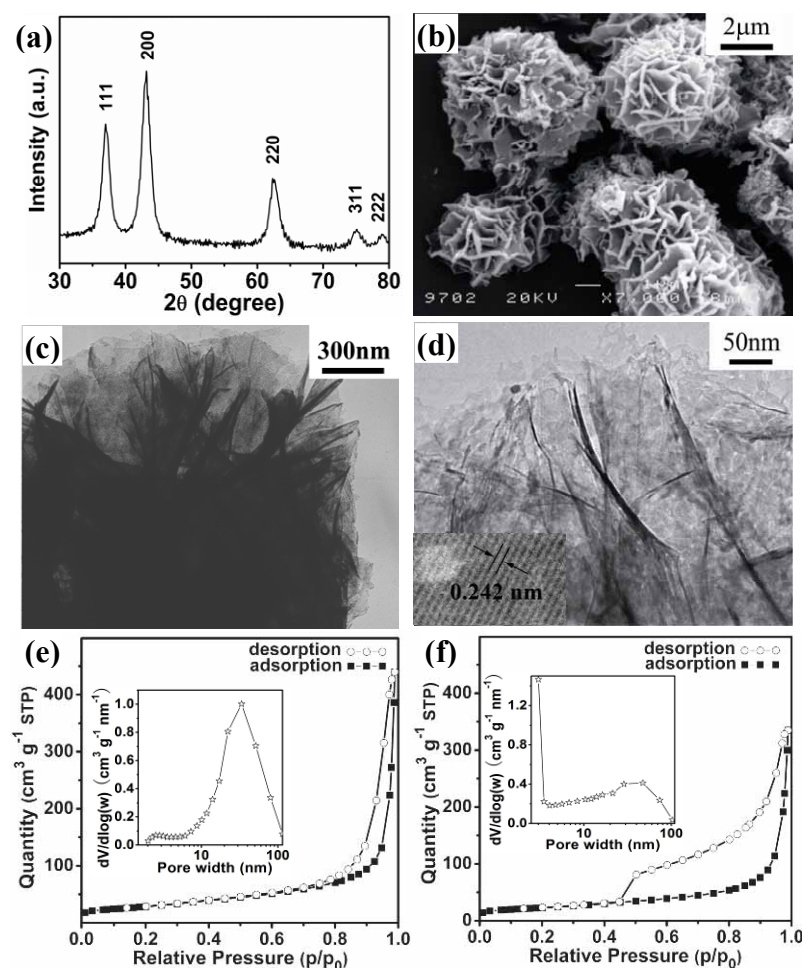


Fig. S3 (a) XRD pattern, (b) SEM image, (c, d) TEM images and (e) N_2 adsorption-desorption isotherms and pore size distribution curve (inset) of the NiO porous microflowers, Inset in (d) is the corresponding HRTEM image, small pores can be clearly observed in the sheets. (f) N_2 adsorption-desorption isotherms and pore size distribution curve (inset) of the precursor for comparison

All the diffraction peaks can be indexed to NiO (JCPDS no. 47-1049), indicating the flowerlike Ni-based precursor is completely decomposed in air, giving rise to the highly pure NiO product (Fig. S3a). The microflowers consist of the stacked porous thin nanosheets with the sheet-thickness of several nanometers and the wide pore width mainly in range of 5~100 nm, and the distance between two neighboring fringes is about 0.242 nm in well accordance with the d_{111} value of cubic NiO (Fig. S3b-e). The BET surface area and pore volume of the porous NiO microflowers are $101.8 \text{ m}^2 \text{ g}^{-1}$ and $0.7 \text{ m}^3 \text{ g}^{-1}$ respectively, larger than the corresponding ones of the Ni-based precursor (Table S1). These result from the formation of

the abundant pores with the width mainly in the range of 5~100 nm on the sheet surface, as revealed by the pore size distribution curves (insets of Fig. S3e, f).

Table S1. BET surface area and pore structure parameters from the N₂ adsorption/desorption experiments.

Samples	BET surface area [m ² g ⁻¹]	Average pore width [nm]	Pore volume [m ³ g ⁻¹]
Ni-based Precursor	81.0	8.2	0.5
NiO-340°C	101.8	20.2	0.7
Ni-335°C	24.5	20.1	0.1
Ni-400°C	2.9	22.2	0.02

SI-4. Typical SEM image of Ni-335°C sample

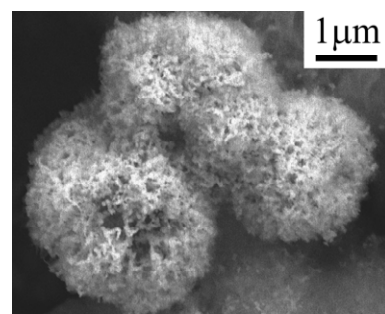


Fig. S4 SEM images of Ni-335°C. The morphology of Ni-335°C is similar to the corresponding precursor shown in Figure 1c.

SI-5. In situ DTG curves and MS spectra in calcining the precursors in Ar and air

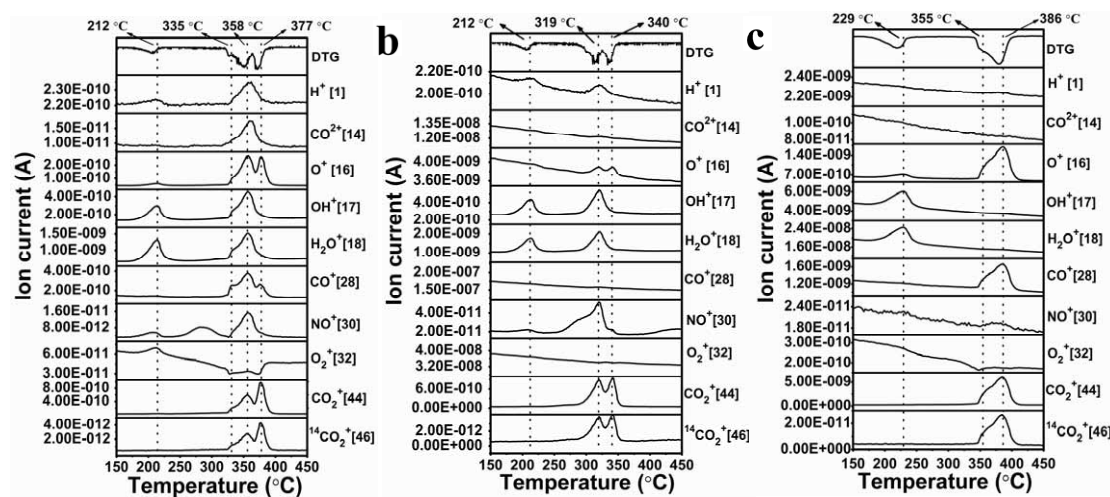


Fig. S5 MS spectra and DTG curves in situ recorded in the calcination process of the Ni-based precursor in Ar (a) and air (b). For comparison, similar experiment was also performed

for the control precursor of $\text{NiC}_2\text{O}_4 \cdot 2\text{H}_2\text{O}$ in Ar (c). The species with amu of 1, 17 and 18 come from H_2O ; 44 and 46 from CO_2 ($^{14}\text{CO}_2$); 16 from O of CO and CO_2 (complicated by O^+ from NO and O_2^{2+} from O_2); 32 from O_2 ; 14 and 28 from CO (14 complicated by N^+ from NO); 30 from NO (complicated by $^{14}\text{CO}^+$ in 355~377 °C).

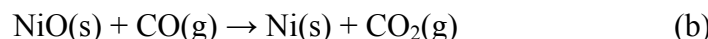
In Ar, the signals around 212 °C result from the release of the crystal water and the slight decomposition of NO_3^- intercalated in Ni(OH)_2 layers, as reflected by the ion peaks for H_2O (1, 17, 18 amu), and a little NO (30 amu) and O_2 (32 amu), respectively. In 325~390 °C, there are two evident peaks in DTG curve. The first one at 358 °C with a shoulder around 335 °C should come from the reduction of Ni(OH)_2 by the intercalated HCHO, i.e.,



as supported by the detected H_2O , CO ($^{14}\text{CO}^+$) (14, 16, 28, 30 amu) and CO_2 (16, 44, 46 amu) (Fig. S5a). The peak around 377 °C is attributed to the decomposition of NiC_2O_4 , i.e.,

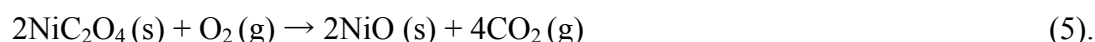
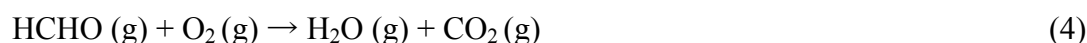


as supported by the detected CO_2 and the accompanied CO species, as well as the absence of H_2O . Actually, we can not exclude the possibility that CO may partially come from the consecutive two-step decomposition of NiC_2O_4 , i.e.,



In this case, CO from the pyrolysis of oxalate (a) also makes the contribution to the formation of the Ni product (b). The negative peak of O_2 (32 amu) is associated with the consumption of the trace O_2 by HCHO and/or CO. It is noted that the decomposition of the control precursor of $\text{NiC}_2\text{O}_4 \cdot 2\text{H}_2\text{O}$ shows a peak starting at 343 °C in the DTG curve (Fig. S5c). Therefore, the first peak in Fig. S5a (at 358 °C with a shoulder around 335 °C) might also be partially contributed from the decomposition of NiC_2O_4 . Hence, the reduction of Ni (II) by reductive HCHO and/or CO in Ar contributed to the formation of Ni nanostructures (see Fig. 3 in the main text).

In air, similar results are obtained except for the whole shift of the ion peaks to the low-temperature side in the range of 293~348 °C, and the absence of the CO species and the negative ion peak for O_2 due to the abundant O_2 . The two peaks in DTG curve mainly come from the following reactions, i.e.,



As shown in Fig. S5b, the first peak at 319 °C comes from the decomposition of Ni(OH)_2 (Reaction 3), the oxidation of the intercalated HCHO (Reaction 4) and the decomposition of the intercalated NO_3^- producing NO and O_2 , as supported by the corresponding MS peaks for H_2O , CO_2 and NO. The second peak at 340 °C is from the decomposition of NiC_2O_4 in the

presence of O₂ (Reaction 5). Hence, the decomposition of Ni(OH)₂ and NiC₂O₄ in air generated the NiO nanostructures (Fig. S3).

By comparing the cases in Ar and air, it is learnt that Ni is generated in Ar, and NiO in air. In detail:

(1) Below 212 °C, the same process occurred for the precursor in Ar and air, i.e., the crystal water was released accompanied by the slight decomposition of the NO₃⁻ intercalated in Ni(OH)₂ layers, leading to a weight loss of ~6.8% (see Fig. 2 in the main text).

(2) In both Ar and air, the decomposition of the intercalated NO₃⁻ ions occurred in a wide temperature range as learned from the detected NO molecules.

(3) In Ar, Ni species was generated from the reduction of Ni (II) by HCHO and/or CO with releasing CO, CO₂ and H₂O (Reaction 1 and 2. Reaction 2 may also occur by consecutive two steps). In air, NiO species was generated from the decomposition of Ni(OH)₂ and NiC₂O₄, with releasing CO₂ and H₂O (Reaction 3-5).

SI-6. Magnetic properties of the Ni nanostructures

Table S2. Saturation magnetization (M_s), remanent magnetization (M_r) and coercivity (H_c) of Ni-335°C and Ni-400°C.

Samples	M _s [emu g ⁻¹]	M _r [emu g ⁻¹]	H _c [Oe]
Ni-335°C	40.2	16.5	192.9
Ni-400°C	51.9	13.2	142.4

SI-7. Characterization on Ni-335°C catalyst after reaction

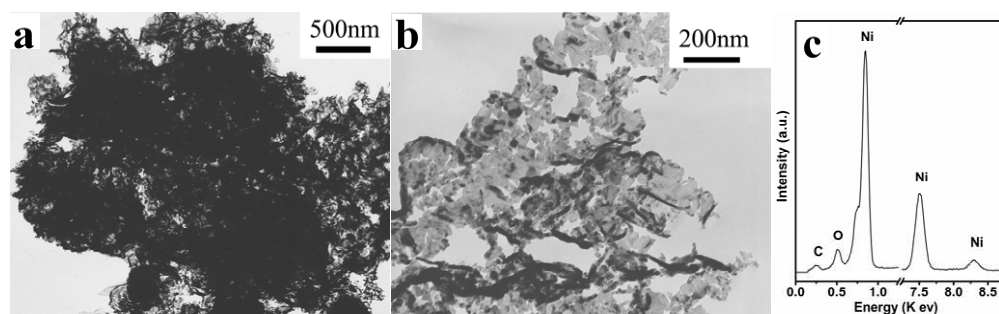


Fig. S6 (a, b) TEM images of the Ni-335°C catalyst magnetically separated from the reaction system after 8 cycles. It is shown the morphology was roughly remained. (c) the corresponding EDX spectrum. C comes from the conductive gel and O from the surface oxidation.

Ni-335°C catalyst was analyzed by inductively coupled plasma mass spectrometry (ICP-MS, ELAN9000) before and after 1 and 6 cycles' reaction, giving the Ni content of 97.2%, 93.4% and 94.3%, respectively. These values are within the error range of ICP-MS analysis.

This implies that the surface of the porous Ni nanostructures was stabilized by oxide layer and no obvious change occurred during the catalytic reaction, which is actually the reason for the superb recycling stability.

These characterization results indicate the high stability of the porous hierarchical Ni nanostructures.

Reference

- 1 P. Jeevanandam, Y. Koltypin and A. Gedanken, *Nano Lett.*, 2001, **1**, 263-266.
- 2 G. T. Duan, W. P. Cai, Y. Y. Luo and F. Q. Sun, *Adv. Funct. Mater.*, 2007, **17**, 644-650.
- 3 L. P. Xu, Y. S. Ding, C. H. Chen, L. L. Zhao, C. Rimkus, R. Joesten and S. L. Suib, *Chem. Mater.*, 2008, **20**, 308-316.
- 4 C. Tessier, L. Guerlou-Demourgues, C. Faure, A. Demourgues and C. Delmas, *J. Mater. Chem.*, 2000, **10**, 1185-1193.
- 5 M. A. Gabal, A. A. El-Bellihi and S. S. Ata-Allah, *Mater. Chem. Phys.*, 2003, **81**, 84-92.
- 6 G. R. Fu, Z. A. Hu, L. J. Xie, X. Q. Jin, Y. L. Xie, Y. X. Wang, Z. Y. Zhang, Y. Y. Yang and H. Y. Wu, *Int. J. Electrochem. Sci.*, 2009, **4**, 1052-1062.